Journal of Materials Chemistry C

RSC Publishing

PAPER

View Article Online
View Journal | View Issue



# Understanding the defect chemistry of tin monoxide

Cite this: *J. Mater. Chem. C*, 2013, **1**, 8194

Jeremy P. Allen,*[a] David O. Scanlon,[bd] Louis F. J. Piper[c] and Graeme W. Watson*[a]

Received 20th September 2013
Accepted 31st October 2013

DOI: 10.1039/c3tc31863j

www.rsc.org/MaterialsC

Tin monoxide has garnered a great deal attention in the recent literature, primarily as a transparent p-type conductor. However, due to its layered structure (dictated by non-bonding dispersion forces) simulation *via* density functional theory often fails to accurately model the unit cell. This study applies a PBE0-vdW methodology to accurately predict both the atomic and electronic structure of SnO. Empirical van der Waals corrections improve the structure, with the calculated *c*/*a* ratio matching experiment, while the PBE0 hybrid-DFT method gives accurate band gaps (0.67 and 2.76 eV for the indirect and direct band gaps) and density of states which are in agreement with experimental spectra. This methodology has been applied to the simulation of the native intrinsic defects of SnO, to further understand the conductivity. The results indicate that n-type conductivity will not arise from intrinsic defects and that donor doping would be necessary. For p-type conduction, the Sn vacancy is seen to be the source, with the 0/−1 transition level found 0.39 eV above the valence band maximum. By considering the formation energies and transition levels of the defects at different chemical potentials, it is found that the p-type conductivity is sensitive to the O chemical potential. When the chemical potential is close to its lowest value (−2.65 eV here), the oxygen vacancy is stabilized which, whilst not leading to n-type conduction, could reduce p-type conduction by limiting the formation of hole states.

## 1 Introduction

Tin monoxide has been investigated for a range of technological applications, including as a gas sensor, an anode material in Li-ion batteries and as a catalyst for some organic cyclization, polymerization and degradation reactions.[1–3] SnO thin films were first reported to show p-type character in 2001,[4] which led to them being tested for use in thin-film transistors (TFTs) in 2008.[5] Oxide semiconductor thin-films have advantages over hydrogenated amorphous silicon and organic-based semiconductors for use in TFTs in that they can often be formed at lower temperature, typically have higher carrier mobilities, can be made more uniform and are amenable to large-area fabrication due to the preparation methods they make available, such as sputtering.[5–9] Most oxide semiconductors which exhibit high carrier mobilities, however, are natively n-type. This is because they typically possess a deep valence band maximum (VBM) that is composed of localized oxygen p states. The depth of the VBM from the vacuum level makes hole generation energetically unfavourable, while the localized O 2p-orbitals result in poor dispersion and large hole effective masses.[10–12] The conduction band maximum (CBM), on the other hand, is in some cases composed of overlapping unoccupied metal s states, making it dispersive and conducive to n-type conduction.[13]

In 1997, Hosono and co-workers published a working hypothesis for generating wide band gap p-type semiconductors based on a parent material of $Cu_2O$.[14,15] The p-type properties were thought to arise from the fact that the covalency of the Cu–O bonds would give a VBM composed of hybridized Cu d and O p states, facilitating hole doping and hole mobility. This led to the formation of a range of new transparent p-type oxides including $CuMO_2$ ($M$ = B, Al, Ga and In), LaCuO$Ch$ ($Ch$ = S, Se and Te) and $SrCu_2O_2$.[5,14–30] However, efforts to fabricate these kind of materials into working p-channel TFTs was limited due to problems with hole mobilities and densities. In addition to producing p-channel TFTs, there is also a desire to generate bipolar TFTs which display both n- and p-type properties within the same device. Of the aforementioned Cu-based materials, no n-type conduction has been achieved, with the exception of $CuInO_2$ which showed electron conduction through the unoccupied In s states.[31] The deficiencies of these Cu-based materials led to the hypothesis that a material which possessed a VBM of spatially spread metal s states would exhibit higher hole mobilities and be a stronger p-type semiconductor. This kind of electronic structure is typical of a range of heavy metal ions which possess valences of two less than the nominal group valence, such as Pb, Bi and Sn, so-called 'lone pair' materials.[32,33]

Modelling studies have played a significant role in understanding the underlying electronic structure of these lone pair materials. The classical inert pair effect considers lone pairs as a

[a]*School of Chemistry and CRANN, Trinity College Dublin, Dublin 2, Ireland. E-mail: allenje@tcd.ie; watsong@tcd.ie*

[b]*University College London, Kathleen Lonsdale Materials Chemistry, 20 Gordon Street, London, WC1H 0AJ, UK*

[c]*Department of Physics, Applied Physics and Astronomy, Binghamton University, Binghamton, New York 13902, USA*

[d]*Diamond Light Source Ltd., Diamond House, Harwell Science and Innovation Campus, Didcot, Oxfordshire, OX11 0DE, United Kingdom*

chemically inert electron pair residing in a hybrid-sp non-bonding orbital which is stereochemically active creating structural distortion.[34–36] In SnO, for example, this lone pair and structural distortion gives rise to a layered litharge structure (detailed in Fig. 1), with the lone pairs directed toward the interlayer separation.[37] However, contrary to classical theory, SnTe possesses a cubic rock salt structure with no structural distortion. Studies led by Watson and co-workers[33,38–42] used density functional theory (DFT) simulation to investigate the formation of classical 'lone pairs' in such materials. These studies showed that bonding between the cation s and anion p states gives rise to bonding and anti-bonding states, with the later forming the VBM. These anti-bonding states are then stabilized by mixing with the cation p states, giving rise to asymmetric electron density and structural distortion. However, when progressing down the chalcogenide series, the anion p states were seen to raise in energy relative to the cation s states, resulting in a weaker contribution of the cation s states to the VBM and thus a weaker lone pair. The weakening lone pairs means that for the later chalcogenides, the increase in energy resulting from the reduced coordination can out-weigh the energy gain from distorting the structure, causing a symmetric structure to result. This revised lone pair model has since been corroborated by other simulation[43–49] and mixed simulation/experimental studies[32,50–53] on these and related materials. SnO possesses a VBM that is composed primarily of hybridized Sn s and O p states and has shown considerable promise as a p-type conductor.[5,54] The composition of the valence band (VB) is not the only requirement for p-type conduction, however, as PbO shows n-type conduction[55] and the Bi 6s states in Bi-containing materials, such as BiCuO*Ch*, are often deep and play no role in the VBM.[56–58]

Although previous simulation studies have afforded a good description of the bonding in SnO, the prediction of the atomic structure has been less satisfactory. This is typically observed by an over-prediction of the *c* lattice vector relative to the *a* vector,[40,42,59,60] caused by the van der Waals interactions that exist between the layers in the structure. The electronic structure methods typically employed in the simulation of solids, such as Hartree–Fock, DFT and hybrid-DFT, are known to fail to account for such dispersion forces[61–63] and have also been seen to cause similar discrepancies in other layered materials, such as $V_2O_5$ (ref. 64 and 65) and $MoO_3$.[66,67] Furthermore, as the band gap has been shown to be dependent on the *c*/*a* ratio, the poor structural prediction can introduce additional inaccuracy into the prediction of the electronic structure.[68,69] To improve structural reproduction, a range of different approaches to include dispersion interactions have been proposed.[62,63,70–73] Duan[74] modelled both the bulk and surface structure of SnO using the approach of Wu and Yang[63] but the reported lattice parameters only showed limited improvement. More recently, Govaerts *et al.* used a non-local van der Waals functional to model SnO, but whilst reasonable agreement was seen for the lattice vectors and volume, the *c*/*a* ratio was still 1.5% too small.[75] In our previous work,[76] we detailed the use of an additive dispersion correction with the PBE-vdW method (to be detailed later) and compared it to an alternative approach of Grimme.[72] Whilst the method of Grimme (PBE-D2) failed to give an accurate structure, the PBE-vdW approach provided excellent agreement of the lattice parameters and bond lengths with experiment. However, due to the discontinuity problem inherent in standard generalized gradient approximation (GGA) methodologies,[77] the band gap was severely underestimated.

To understand the link between the structure, stoichiometry, transparency and p-type conductivity, as well as investigating the material for bipolar capabilities, the electronic structure and defect chemistry has been further investigated. Previous experiment has suggested that the SnO VBM is 5.8 eV below the vacuum level,[54] similar to other p-type materials, such as $Cu_2O$ (~5.6 eV) and Li-doped NiO (~5.5 eV).[78,79] More recent experiments, however, have revised this to being VBM 4.9 eV below the vacuum level.[80] The direct optical band gap is found to be ~2.7 eV, giving moderate transparency; however, SnO also has an indirect fundamental band gap of 0.7 eV.[5] This means that the CBM resides 5.1 eV below the vacuum level, or 4.2 eV from the result of Quackenbush *et al.*, which are at similar positions to the CBM in n-type materials, such as ZnO (~4.1 eV) and $In_2O_3$ (~5.2 eV).[78,79] As mentioned previously, simulation studies using GGA have underestimated the band gaps of SnO, with values of the indirect gap ranging from 0.02 (ref. 76) to 0.6 eV (ref. 40) (depending on the exact functional and methodology used) and values of ~2.0 eV are reported for the direct gap.[60,81] From band structure calculations,[76,82] the VBM is seen to be reasonably flat, with a DFT-calculated hole effective mass of $2.05m_e$,[54] while the CBM is more disperse,[60,76,81] likely possessing a small electron effective mass, and is suggestive of a reasonable n-type properties. Doping with Y and Sb has also been shown to offer improved p- and n-type properties, respectively,[78,83,84] and, consequently, devices which show bipolar operation have been reported, although the mechanism of p-type enhancement by Y is unclear.[79,85]

Tin monoxide is metastable[86,87] meaning that thin films can often contain impurities of Sn metal, $SnO_2$ and other intermediate oxides and hence a range of approaches have been employed to

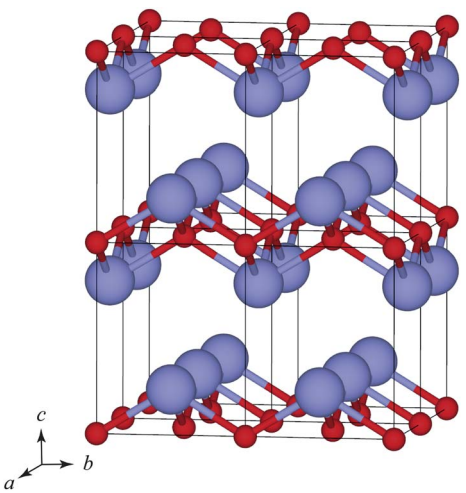


**Fig. 1** Atomic structure of tin monoxide. The unit cell is expanded 2 × 2 × 2 for clarity. Tin and oxygen atoms are coloured blue and red, respectively.

obtain SnO of high purity. Cao and co-workers[83–85,88,89] favour a two-step process involving the electron beam evaporation (EBE) of $SnO_2$ on p-type silica, followed by thermal annealing at temperatures between 300 and 600 °C. Conversely, the epitaxial process used by Hosono and co-workers[5,54,78,79] involves pulsed laser deposition (PLD) onto (001) yttria-stabilized zirconia surfaces. Other techniques include sputtering[9] and solution-based spin coating.[90] The highest Hall-effect mobilities ($\mu_H$) and hole concentrations ($N_H$) are typically reported using the EBE method, with Liang *et al.*[84] reporting values of $\mu_H = 3.9\ cm^2\ V^{-1}\ s^{-1}$ and $N_H = 0.56 \times 10^{16}\ cm^{-3}$. PLD-formed epitaxial films often exhibit lower values, with Ogo *et al.* reporting 2.4 $cm^2\ V^{-1}\ s^{-1}$ and $2.5 \times 10^{17}\ cm^{-3}$, respectively.[5] TFTs generated using the PLD-grown films have shown a field-effect mobility ($\mu_{FE}$) of 1.3 $cm^2\ V^{-1}\ s^{-1}$,[5,54] while TFTs using thin-films generated *via* sputtering or the spin coating method gave comparable but smaller values of $\mu_{FE}$, 0.24 (ref. 9) and 0.13 $cm^2\ V^{-1}\ s^{-1}$,[90] respectively. However, unlike the latter approaches, EBE and PLD are suggested to be less amenable to large-scale device production.[9] Experimental thin films are often found to have a degree of off-stoichiometry, exhibited as a small cation deficiency/oxygen excess.[4,83,91] Togo *et al.*[60] and Oba *et al.*[92] both used a GGA DFT approach with Perdew–Wang-91 (PW91) functionals, to consider the native intrinsic defects. Their results suggested that the Sn vacancy would dominate under oxygen-rich conditions, forming shallow acceptor states and giving rise to the observed p-type conductivity. The O interstitial had a lower formation energy and hence would exhibit a higher equilibrium concentration than the Sn vacancy at high temperature. However, the O interstitial was not expected to ionize and therefore would not contribute to the p-type conductivity. The donor-type defects were predicted to be of sufficiently low concentration as to not compensate the holes generated by the Sn vacancies.

Although the work of Togo *et al.*[60] and Oba *et al.*[92] provides results for the native defects in SnO, discrepancies remain. The lack of dispersion corrections mean that the unit cell used in their defect simulations was distorted. Not only will this affect the band gap and electronic structure of the material, it may also erroneously influence the defects. Previous work on both p-type[29,93–95] and n-type[96–101] materials have also shown that standard GGA methods favour artificial electron delocalisation, which can result in shallow defect transition levels. Thus a higher level of theory is needed to accurately model the defect chemistry of a material. To this end, the aim of this study is two-fold. Firstly, it will accurately model both the ionic and electronic structures simultaneously for the first time by applying a van der Waals correction to a hybrid-DFT (PBE0-like) functional. Comparison will be made to both experimental[80] and previous simulation results, which used a PBE-vdW methodology to afford an excellent reproduction of the physical structure but failed to correctly predict the electronic structure.[76] Secondly, the intrinsic defects in SnO will be simulated in both neutral and charged states using this hybrid-DFT approach with dispersion corrections. This will allow a full description of the native defects, with a higher degree of accuracy than has been achieved previously, allowing for a complete discussion of the native p- and n-type defects.

## 2 Methodology

### 2.1 DFT-vdW methodology

All simulations in this study have been conducted using the periodic-DFT code VASP.[102,103] A plane-wave basis set is used to describe the valence electronic states (Sn: [$5s^2$, $5p^2$], O: [$2s^2$, $2p^4$]), with the projector-augmented wave[104,105] method employed to describe their interactions with the core states. A number of trial calculations were also run with the Sn $4d^{10}$ states considered as valence, and they will be discussed within the results section. One approach to improve on the delocalised defects states, shallow transition levels and the inherent band gap problem of GGA methodologies[77] is to use a hybrid-DFT methodology. The popular PBE0 (ref. 106 and 107) and screened HSE06 (ref. 108 and 109) approaches, which are based on the Perdew–Burke–Ernzerhof (PBE)[110] functional, work by replacing a portion of the PBE exchange ($E_x^{PBE}$) with exact-Fock exchange ($E_x^{Fock}$):

$$E_{xc}^{PBE0} = aE_x^{Fock} + (1 - a)E_x^{PBE} + E_c^{PBE} \quad (1)$$

In the formal PBE0 and HSE06 methodologies, $a$ is fixed at 0.25. The PBE0 and HSE06 methods differ in that the HSE06 formalism includes a screening length (0.11 $bohr^{-1}$) to split the exchange term into short- and long-range components, with only the short-range component replaced by a portion of Fock exchange. These hybrid methods have been extensively used in plane-wave calculations in recent years and, although they are more computationally demanding than the PBE method, they have been shown to provide a closer fit to experimental data for a range of systems. This has included the prediction of the atomic and electronic structure (including band gaps),[111–115] optical transitions,[116–119] as well as defective[28,120,121] and magnetic[122–124] systems. There is no particular percentage of exact Fock exchange that is applicable to all systems,[107] however, and a number of studies using the related screened HSE functional have reported that closer agreement to experiment can be obtained for material properties by tuning this percentage, typically to reproduce the experimental band gap. This has been demonstrated for the electronic structures and defect properties of a range of oxide materials, including ZnO, $SnO_2$, $TiO_2$, $Ga_2O_3$, $In_2O_3$, MgO, $Al_2O_3$, $SiO_2$ and $Cu_2O$.[125–128] Therefore, we have adjusted the percentage of exchange to provide optimal descriptions of the indirect and direct fundamental band gaps assuming the experimental structure, *i.e.*, independent of the effect of dispersion corrections. The amount of exchange found using this approach was 15% and thus this has been used throughout (unless otherwise stated). As this is different to the formal PBE0 methodology, the approach is only PBE0-like in nature; however, for simplicity it will be referred to solely as PBE0 herein. The HSE06 method was also tried but it was found to give a greater difference between the indirect and direct fundamental band gaps. Therefore, the only hybrid-DFT approach reported here and used for the defect calculations was that of PBE0.

The DFT-vdW approach, outlined previously using with the PBE functional (PBE-vdW),[76] acts by correcting the self-consistent Kohn–Sham DFT energy, $E_{KS\text{-}DFT}$, with the addition of an empirical dispersion term, $E_{disp}$. The dispersion-corrected energy, $E_{DFT\text{-}vdW}$, is therefore represented as

 

$$E_{\text{DFT-vdW}} = E_{\text{KS-DFT}} + E_{\text{disp}} \quad (2)$$

The additive term in this approach makes it both flexible and simple, allowing it be used with a range of different density functionals. It can also be easily tuned for a large variety of systems, through the adjustment of parameters based on empirical or semi-empirical physical quantities. From a procedural point of view, the simplicity also means that it can be used for large or complex systems without becoming prohibitively expensive.

The dispersion term itself is determined by

$$E_{\text{disp}} = -s_6 \frac{C_6^{ij}}{R_{ij}^6} f_{\text{dmp}}(R_{ij}) \quad (3)$$

where $R_{ij}$ is the distance between atoms $i$ and $j$, $C_6^{ij}$ is the dispersion coefficient between the same atoms and $s_6$ is a scaling factor reflecting the fact that DFT functionals may include a portion of long-range attraction.[71] The damping function is used to reproduce the reduction in van der Waals attraction as two atoms are brought together and their charge densities overlap. As the overlap increases, the polarizability reduces, and hence so do the dispersion forces. The damping function is given by

$$f_{\text{dmp}}(R_{ij}) = \frac{1}{1 + e^{-4B\left(R_{ij} - R_r^{ij}\right)}} \quad (4)$$

where $B$ is the damping parameter, which is related to the slope of the function, and $R_r^{ij}$ is an equilibrium distance used to control the distance that the damping acts over. This damping function results in the dispersion interactions being reduced to 50% of their undamped value when the interatomic separation is equal to $R_r^{ij}$.

The parameter set used in the dispersion corrections are detailed in Table 1. The dispersion coefficients, $C_6^{ij}$, taken from the work of Madden and co-workers, are determined from Hartree–Fock-calculated ionic polarizabilities.[129,130] To define $R_r^{ij}$, different values from the experimental structure[131] were used depending on the functional. For PBE-vdW, the experimental in-layer distances were used for the Sn–O and O–O distances, whilst the experimental across-layer distance was used for the Sn–Sn.[76] The PBE0 approach, as shown later, reproduces the nearest-neighbour bond distances and thus any applied correction would erroneously affect them. Therefore, the mid-point between the experimental in-layer and across-layer distances were used to represent all dispersion forces in SnO with PBE0, so that the nearest-neighbour interactions were fully damped whilst the next nearest-neighbour interactions were undamped. The value of $B$ (0.5 Å$^{-1}$) was determined by plotting the damping function and selecting the largest value which did not cause a reversal in the sign of the force, *i.e.* making it negative, thus ensuring the damping function did not affect interactions with atoms beyond $R_{ij}$. In addition, a cutoff of 20 Å was used for all interactions. For PBE-vdW, the optimal value of $s_6$ was determined to be 65% through fitting to the experimental structure. The value of $s_6$ was analysed for PBE0-vdW with 15% exchange and 65% was again found to give the closest fit to the experimental structure and, therefore, it was not adjusted further.

**Table 1** Parameters used in the DFT-vdW methods for modelling SnO

| Ion pair | $C_6^{ij}$ (eV Å$^6$) | $R_r^{ij,\text{PBE}}$ (Å) | $R_r^{ij,\text{PBE0}}$ (Å) |
|---|---|---|---|
| Sn–Sn | 73.07 | 3.693 | 3.693 |
| Sn–O | 74.45 | 2.222 | 3.184 |
| O–O | 77.34 | 2.688 | 3.762 |

To determine the equilibrium lattice parameters, the bulk unit cell was minimized at a series of different volumes, with both the lattice vectors and cell angles allowed to relax fully within the constraint of a constant volume. The resultant energy–volume curve was then fitted to the Murnaghan equation of state[132] to determine the equilibrium cell volume. This approach minimizes potential problems with Pulay stress and changes in basis set which can accompany volume changes in plane-wave calculations. Although the Pulay stress can be anisotropic, the accuracy of this approach was previously confirmed for SnO using PBE-vdW with the Murnaghan-fitted structure at a plane-wave cutoff of 500 eV. The optimized unit cell was re-run with a higher plane-wave cutoff of 1000 eV and the pressure along different lattice vector directions was compared, with the Pulay stress found to be isotropic. A plane-wave cutoff of 500 eV was used, with Monkhorst–Pack[133] $k$-point grids of $6 \times 6 \times 3$ and $2 \times 2 \times 1$ used for the unit cell and the $3 \times 3 \times 3$ supercell, respectively. For each of the bulk calculations, the forces were deemed to be converged when they were less than 0.001 eV Å$^{-1}$ and the pressure was less than 0.127 kBar. This is required for the bulk optimizations as the weak van der Waals forces along the $c$ axis requires high accuracy to locate the minimum. For the defective supercell calculations, a constant volume regime was applied with fixed unit cell dimensions, and therefore, the convergence criteria on the forces were relaxed to 0.01 eV Å$^{-1}$, as done previously for SnO.[76] The energies of bulk $\alpha$-Sn metal and $SnO_2$ were determined using Monkhorst–Pack $11 \times 11 \times 11$ and $4 \times 4 \times 4$ $k$-point grids, respectively. For gaseous $O_2$, the molecule was simulated in the triplet state within a large $16 \times 16 \times 16$ Å cell with a single $k$-point at $\Gamma$.

The optical absorption spectrum, as well as the optical transition matrix, was calculated within the transversal approximation.[134] This approach determines the optical absorption by summing all direct VB to conduction band (CB) transitions on the $k$-point grid and does not include indirect and intraband transitions.[135] To improve the accuracy of the optical calculation, the $k$-point grid was increased to a $\Gamma$-centred $8 \times 8 \times 4$ mesh. As only single-particle transitions are included, any electron–hole correlations would require higher-order electronic structure methods;[136,137] however, this approach has been shown to provide reasonable optical absorption spectra in comparison to experiment.[117,138–143]

All structural figures were generated using the visualization package VESTA.[144]

### 2.2 Defect calculations

To calculate the formation energy of defect $D$ with charge $q$, $\Delta E_f$ ($D$, $q$), the following equation[145,146] was used:

$$\Delta E_f(D,q) = E_{\text{defective}}(D,q) - E_{\text{pure}} + \sum_i n_i(E_i + \mu_i) + q(E_{\text{Fermi}} + \varepsilon_{\text{VBM}}^{\text{pure}}) + E_{\text{align}}[q] \quad (5)$$

where $E_{\text{defective}}(D, q)$ is the total energy of the supercell containing the defect and $E_{\text{pure}}$ is the energy of the pure supercell. $E_i$ is the energy of species $i$ in its standard state, for this study specifically it refers to a Sn atom in bulk $\alpha$-Sn and an $O_2$ molecule. For each of these species, identical dispersion corrections were applied as were used for modelling SnO. The number of atoms of type $i$ added to or removed from an external reservoir is given by $n_i$, and $\mu_i$ is the chemical potential of species $i$. The final two terms in eqn (5) refer to corrections for charged defect cells and will simply equal zero for a neutral system. $E_{\text{Fermi}}$ is the Fermi energy, ranging from the VBM at 0.0 eV up to the CBM, and $\varepsilon_{\text{VBM}}^{\text{pure}}$ is the eigenvalue of the VBM in the bulk material. The final term accounts for both the alignment of the electrostatic potential between the bulk and defective charged supercells and finite-size effects which can occur in the calculation of charged impurities, as outlined by Freysoldt *et al.*,[147] using a dielectric constant of $\varepsilon_0 = 5.95$.[84] The average dielectric constant calculated using a $G_0W_0$ approach was 6.12, which is in good agreement with the experimental value. The Fermi energy for the thermodynamic transition (ionization) level between two charge states $q$ and $q'$ of a given defect, $\varepsilon_D(q/q')$, is found when their formation energies are equal:

$$\varepsilon_D(q/q') = \frac{\Delta E_f(D,q) - \Delta E_f(D,q')}{q' - q}. \quad (6)$$

### 2.3 Experimental

The SnO films were grown by PLD using similar growth parameters to those reported by Hosono *et al.*[78] X-ray diffraction of the PLD films showed that the lattice constants $a$ and $c$ were 3.8011 Å and 4.8351 Å. The 100 nm films displayed p-type conductivity with a hole mobility and a hole density of 7.0 $cm^2 V^{-1} s^{-1}$ and $\sim 1 \times 10^{17}$ $cm^{-3}$, respectively. The optical gap was extrapolated to be $\sim$2.6 eV. Further details are given in ref. 80 The bulk electronic structure of these films was measured using a combination of hard X-ray photoelectron spectroscopy (HAXPES) and O K-edge X-ray emission and absorption spectroscopy (XES/XAS) at the National Synchrotron Light Source (NSLS). These results and experimental parameters are reported elsewhere, alongside other experimental spectra, and are used here primarily as a validation of calculated data.[80]

## 3 Results

### 3.1 Atomic structure

Tin monoxide crystallizes in the *P*4/*nmm* space group and is a layered material, as shown previously in Fig. 1. Both the Sn(II) and O ions are 4-coordinate; however, while the anions have a regular tetrahedral geometry, the Sn(II) cations are less regular and the four oxygen ions they bond to form the bottom of a square-based pyramid, with asymmetric electron density occupying the vertex position. The calculated lattice vectors and bond lengths using the hybrid-DFT PBE0 and PBE0-vdW methodologies, alongside experimental values[131] and those calculated using PBE and PBE-vdW[76] are given in Table 2. The PBE0-vdW approach was also used with 4d states considered as valence, investigating their requirement and effect on structural prediction, the results of which are also included in Table 2.

A comparison of the methods with no dispersion corrections, PBE and PBE0 (with 15% and 35% exchange), shows that a distorted structure is found with all approaches. This distortion is observed by an overestimation of the $c$ vector relative to the $a$ vector. The bond lengths show that this results from an overestimation of the across-layer distances, with the in-layer values possessing a more reasonable comparison to experiment. The position of the Sn atom is similar for all approaches, indicating that the methods predict the same basic unit cell structure and distortion, with only the percentage difference to experiment changing. For example, PBE predicts an $a$ lattice vector which is 1.6% larger than experiment, while PBE0 (15%) is more accurate with a percentage difference of 0.6%. This level of agreement is to be expected and is typically seen when comparing DFT and hybrid-DFT approaches.[23,141,142,148] It was possible to approximate the experimental cell volume using a larger amount of exchange (PBE0 with 35%) by exploiting the overbinding associated with Hartree–Fock calculations.[149] However, since this overbinding occurs for all interactions, and the vdW is still not included, this leads to a $c$ axis which is slightly too large, an $a$ axis which is too small and no improvement in the $c/a$ ratio.

The introduction of the dispersion corrections offers a significant improvement. Firstly, the distortion in the unit cell vectors is removed, with both the $a$ and $c$ vectors being very close to experiment. This is further evidenced in the $c/a$ ratio, which is only 0.2% larger than experiment for PBE-vdW and near-exact for PBE0-vdW. Secondly, the bond lengths, both in-layer and across-layer, are seen to closely resemble their experimental equivalents, with the errors being within 0.2%. Finally, the position of the Sn atom is consistent with experiment, indicating that the dispersion-corrected methodologies not only reproduce the experimental unit cell volume and dimensions, but also the underlying atomic structure of the system.

The inclusion of the 4d states to the valence is seen to have a negligible effect on the structural relaxation, with the error to experiment for all measured structural quantities being very similar to those calculated with the 4d states included in the core. Their inclusion increases the length of time and amount of computational resources required to achieve structural relaxation. While there is less impact for a simple bulk unit cell structure, for large supercell structures, this would result in a more resource intensive approach.

The level of agreement between PBE-vdW and PBE0-vdW, as well as their comparison to experiment, is unsurprising considering that both methods use the same parameter sets and that the value of $s_6$, the percentage of dispersion correction to add, was originally fitted to the experiment structure. The results do however highlight the transferability of the parameter set between different computational approaches. Despite the strengths of the PBE-vdW approach for accurately predicting the structure of SnO, its main failing was its inability to correctly

 

**Table 2** Experimental[131] lattice vectors and bond lengths for SnO with those calculated using PBE,[76] PBE-vdW,[76] PBE0 (with both 15% and 35% exchange), and PBE0-vdW (with 15% exchange) methods. The PBE0-vdW(+d) results include the 4d electrons as valence states. Percentage differences to experiment are given in parenthesis and all values are in Å, except cell volume which has units of Å$^3$, the *c*/*a* ratio which is dimensionless and the amount of exchange used with PBE0, which is expressed as a percentage. The *u* value is the fractional coordinate of the Sn atom in the unit cell at (0.0000, 0.5000, *u*).† Indicates reference values which are near identical to the experimental parameters from the thin-films of this study

| Property | PBE[76] | PBE-vdW[76] | PBE0 | PBE0 | PBE0-vdW | PBE0-vdW(+d) | Experiment[131] |
|---|---|---|---|---|---|---|---|
| PBE0 exchange | — | — | 15 | 35 | 15 | 15 | — |
| *a* | 3.860 (1.6) | 3.801 (0.0) | 3.822 (0.6) | 3.777 (−0.6) | 3.804 (0.1) | 3.812 (0.3) | 3.801† |
| *c* | 5.042 (4.3) | 4.843 (0.2) | 5.018 (3.8) | 4.974 (2.9) | 4.840 (0.1) | 4.848 (0.3) | 4.835† |
| *c*/*a* | 1.306 (2.7) | 1.274 (0.2) | 1.313 (3.2) | 1.317 (3.5) | 1.272 (0.0) | 1.272 (0.0) | 1.272† |
| Volume | 75.14 (7.6) | 69.97 (0.2) | 73.29 (4.9) | 70.96 (1.6) | 70.04 (0.3) | 70.43 (0.8) | 69.85† |
| *u* | 0.2300 | 0.2384 | 0.2296 | 0.2298 | 0.2375 | 0.2377 | 0.2381 |
| Sn–Sn (in-layer) | 3.582 (1.2) | 3.543 (0.1) | 3.551 (0.3) | 3.515 (−0.7) | 3.538 (0.0) | 3.546 (0.2) | 3.539 |
| Sn–O (in-layer) | 2.252 (1.4) | 2.224 (0.1) | 2.231 (0.5) | 2.207 (−0.7) | 2.222 (0.0) | 2.227 (0.2) | 2.222 |
| O–O (in-layer) | 2.730 (1.6) | 2.687 (0.0) | 2.702 (0.5) | 2.670 (−0.6) | 2.690 (0.1) | 2.695 (0.3) | 2.688 |
| Sn–Sn (across-layer) | 3.855 (4.4) | 3.694 (0.0) | 3.830 (3.7) | 3.790 (2.6) | 3.701 (0.2) | 3.706 (0.4) | 3.693 |
| Sn–O (across-layer) | 4.336 (4.6) | 4.149 (0.1) | 4.312 (4.0) | 4.272 (3.1) | 4.152 (0.2) | 4.158 (0.3) | 4.145 |
| O–O (across-layer) | 5.042 (4.3) | 4.843 (0.2) | 5.018 (3.8) | 4.974 (2.9) | 4.840 (0.1) | 4.835 (0.3) | 4.835 |

predict the size of the indirect and direct fundamental band gaps,[76] a well-known problem for standard GGA approaches.[77] It is in the electronic structure that the PBE0-vdW approach was therefore expected to show significant improvement over the PBE-vdW method.

### 3.2 Electronic structure

The calculated total (EDOS) and partial (ion and *l*-quantum number decomposed) electronic density of states (PEDOS) determined using the PBE0-vdW methodology with the 4d states in the core are displayed in Fig. 2. To aid in analysis, the VB can be split into three regions of different character. The bottom of the VB, between −10.0 and −8.0 eV, is dominated by Sn s and O p states. The top of the VB, −3.0 to 0.0 eV, is seen to have a similar composition, with some mixing from occupied Sn p states. From previous calculations and analysis by Watson and co-workers, these two regions can be identified as the lone pair, or asymmetric density, formed in many Sn(II) and Pb(II) compounds.[33] The region furthest from the VBM is the bonding combination between the Sn s and O p orbitals, while the region at the top of the VB is anti-bonding in nature. The additional Sn p states in the upper region stabilize the anti-bonding combination, thus allowing the asymmetric density to form and leading to a distorted crystal structure. The section of the VB between these regions is dominated by the O p states, with small contributions from Sn s, p and d states. The CBM is primarily composed of the unoccupied Sn p states, with s, p, d and O 2p states appearing further into the CB.

The EDOS and PEDOS were also calculated with the 4d in the valence, given previously in Fig. 3 ref. 80. From a qualitative view, however, little variation in terms of peak position and magnitude was observed between the two approaches. To further validate the PEDOS determined without the 4d states, the total DOS, occupied O 2p and unoccupied O 2p can be compared to experimental HAXPES, O K-edge XES and XAS spectra, respectively. To enable comparison to be made, the calculated data is weighted according to orbital cross-section and convoluted using a pseudo-Voight function to account for instrumental (Gaussian) and life-time (Lorentzian) broadening, as described previously.[80] Energy alignment between the experiment and calculated spectra was performed for the XES and HAXPES spectra by using the measured O 1s core level and Fermi level energies, respectively. In addition to aligning with the O 1s core-level, a rigid shift towards higher energy is required to compensate for the core-hole final state effect in the XAS.[80] Here, we note excellent agreement between the XAS and the calculated unoccupied O 2p states when a 0.6 eV rigid shift is applied. The excellent agreement between the experiment and calculations given in Fig. 3 validates the simulation results and methodology.

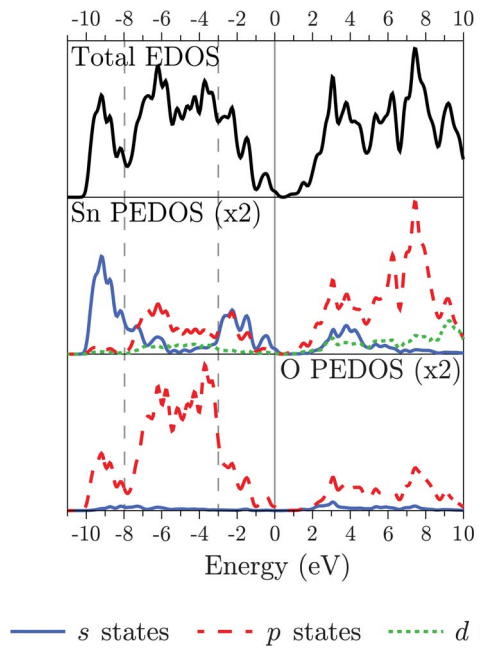


**Fig. 2** The calculated total (EDOS) and partial (ion and *l*-quantum number decomposed) electronic density of states (PEDOS) of SnO. The highest occupied state is set to 0.0 eV.

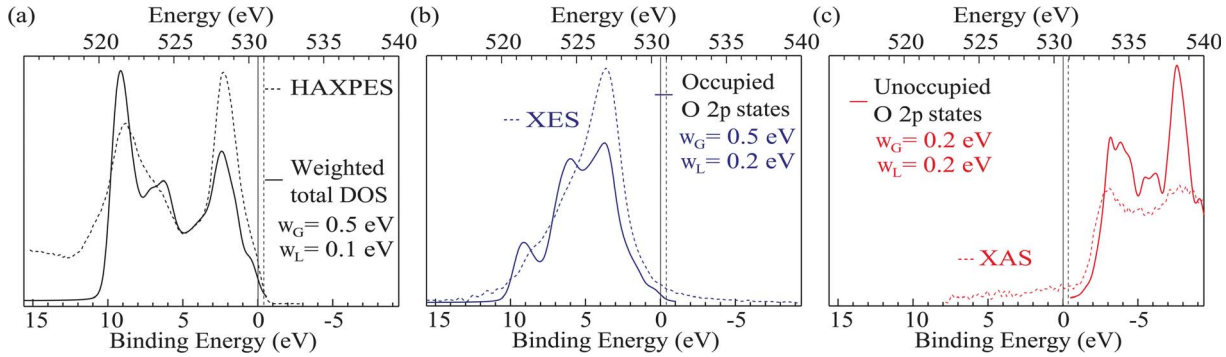


**Fig. 3** Comparison plots of the weighted PBE0-vdW DOS and experiment. (a) Weighted total DOS with HAXPES; (b) weighted occupied O 2p PEDOS with O K-edge XES; and (c) weighted occupied O 2p PEDOS with rigidly core-hole shifted XAS. All calculated plots are solid, while experimental spectra are dashed. The Gaussian and Lorentzian width parameters ($w_G$ and $w_L$, respectively) for deconvolution of the total EDOS and broadening of the PEDOS are given. For the calculated EDOS and PEDOS, the highest occupied state is set to 0.0 eV (solid vertical line), while the experimental Fermi energy (dashed vertical line) is at 531 eV.

The calculated band structure along the high symmetry points[150] is displayed in Fig. 4, with the inclusion of fatband analysis to indicate the contribution to each band from Sn s, p and O p states. The VBM is located just offset from the $\Gamma$-point, at a $k$-point of 0.0405, 0.0405, 0.0000. This is in agreement with the work of Togo *et al.* who state that the VBM is located between the $\Gamma$ and the $M$-points.[60] The CBM is observed at the $M$ point (0.5000, 0.5000, 0.0000) with an energy of 0.67 eV, meaning that SnO is an indirect band gap material. The smallest direct fundamental band gap is also observed at the $M$-point, with an energy of 2.76 eV. Experimental data places the indirect and direct gaps at 0.7 and ~2.7 eV, respectively,[5,88] indicating excellent agreement between experiment and simulation. For comparison, the PBE-vdW method predicts indirect and direct fundamental gaps of 0.03 and 1.94 eV, respectively.[76] Therefore, while both methodologies give similar atomic structures for SnO, the PBE0-vdW technique is required to accurately reproduce the electronic structure. The fatband analysis further corroborates the PEDOS that the top of the VB is comprised of Sn s and O p states, while the bottom of the CB is dominated by unoccupied Sn p states.

The inclusion of 4d as valence states was found to give rise to a band structure which was qualitatively the same as that displayed in Fig. 4(a). A small change in the band gaps was observed though, with the indirect and direct fundamental gaps adjusting to 0.67 and 2.71 eV, respectively. The position of the VBM was also seen to shift slightly, moving to 0.0270, 0.0270, 0.0000; however, the top VB is quite flat around the $\Gamma$-point, with the eigenvalues being of similar energy, and therefore this shift is not significant.

To determine the optical band gap of SnO, the Tauc relation is used:

$$(\alpha h\nu)^n = A(h\nu - E_g^{opt}) \quad (7)$$

where $A$ is a constant, $\alpha$ is the absorption coefficient, $h\nu$ is the photon energy, $E_g^{opt}$ is the optical gap and $n$ is an index which is dependent on the type of electronic transition that the absorption results from and is equal to 2 for an allowed direct transition. This means that the optical band gap can be obtained from a plot of $(\alpha h\nu)^2$ *vs.* $h\nu$ (Fig. 4(d)) by extrapolating $(\alpha h\nu)^2$ to zero.[142,151–154] Extrapolation gives an optical band gap of 2.95 eV. The onset of optical absorption occurs at the $M$ point, the location of the direct fundamental gap, from the highest VB to the CBM but it is very weak. The large increase in optical absorption at ~2.9 eV results from direct VB to CB transitions at

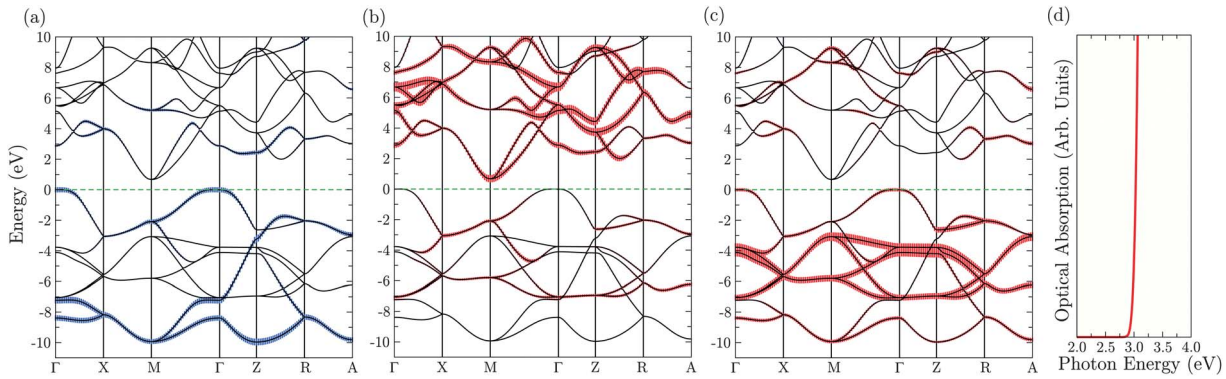


**Fig. 4** The calculated band structure of SnO using fatband analysis to indicate the contribution to each band of (a) Sn s, (b) Sn p and (c) O p states. The optical absorption spectrum, $(\alpha h\nu)^2$ *vs.* $h\nu$, for SnO is given in (d). In the band structures, the valence band maximum is set to 0.0 eV as indicated by the horizontal green dashed line.

positions between the $\Gamma$ and $M$ points. The optical gap of ~2.9 eV is thus the origin of the near-transparency of SnO, despite its smaller fundamental indirect and direct band gaps.

The curvature of the bands at the VBM and CBM relates to the band-edge effective masses of hole states and electrons, respectively. These can therefore be directly used to obtain an estimate of the respective the p/n-type properties. The effective mass, $m^*$, is calculated by

$$\frac{1}{m^*(E)} = \frac{1}{\hbar^2 k}\frac{\mathrm{d}E}{\mathrm{d}k} \quad (8)$$

where $E(k)$ is the band-edge energy as a function of wave vector $k$, taken directly from the calculation.[155] The smaller the band-edge effective mass, the better the expected conductivity. This approach assumes that the bands are parabolic, which clearly does not describe those at the top of the VB; the hole effective mass is therefore not expected to be well-described under a typical semiconductor effective mass description. The bands at the bottom of the CB are more parabolic in nature and should thus be better described. Despite the approximate nature of this approach, the calculated effective masses act as a reasonable guide to the conduction properties, enabling comparisons to be made to other materials, as has been done previously for a large range of p- and n-type materials.[27,117,141,148,156] The calculated hole effective mass at the VBM is found to be $2.60m_e$ ($2.37m_e$ with valence 4d states). This value is reasonably high and is not conducive to good p-type properties, however, the flat nature of the VBM does not make this value surprising. Conversely, the dispersive CBM has a relatively small electron effective mass of $0.27m_e$ ($0.21m_e$ with valence 4d states), suggesting that the inherent electron mobilities of SnO should be stronger than the hole mobilities.

In previous work, Togo *et al.*[60] postulated that p-type conductivity in SnO would occur *via* a hopping mechanism between the asymmetric densities in the interlayer gap, due to anisotropy in their calculated band structure. A similar anisotropy is observed around the VBM in this study, with the energy of the band changing more rapidly with $k$-point from $\Gamma$ towards $Z$ than in the $M$ direction. To explore this further, the charge density of the uppermost VB is plotted in Fig. 5. The partial charge density plots indicate that the asymmetric charge density clouds overlap between layers in the gap, while they are further away from each other moving along the $ab$ plane of a single layer. The analysis of the spatial properties of the asymmetric charge density therefore supports this suggestion.

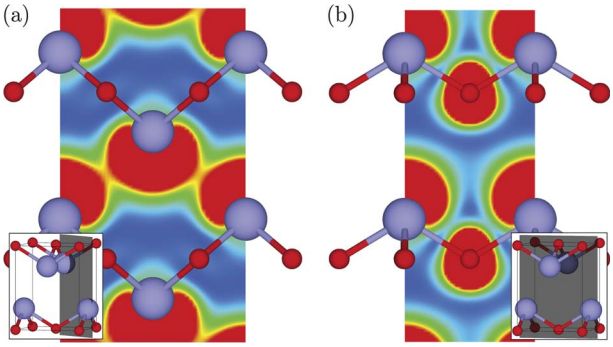


**Fig. 5** Partial charge density of the uppermost valence band in SnO, shown in (a) (110) and (b) (100) planes. Insets show the plane relative to the unit cell. Large blue and small red spheres indicate Sn and O atoms, respectively. The charge density ranges has limits of 0.000 (blue) and 0.035 e Å$^{-2}$ (red).

### 3.3 Neutral and charged defects

The characterization of bulk SnO indicated that the atomic and electronic structure can be adequately described with the 4d states being confined to the core. Therefore, to avoid the large increase in computational cost that their inclusion as valence electrons in supercell calculations would require, all defects have been modelled with the 4d states treated as core electrons.

Four intrinsic defects were modelled: the cation and anion vacancies and interstitials. Within the SnO structure two interstitial positions exist, which have coordination environments of four and five. In accordance with the work of Togo *et al.*,[60] the former of these was the least stable, and therefore all mention of interstitial defects refers to the five coordinate site, as shown in Fig. 6(a). The four-coordinate interstitial positions were modelled in their neutral charge state but were higher in energy for both the Sn and O interstitial defects. The atomic displacements and bond length changes of the neutral defective cells are detailed in Table 3 and Fig. 6.

The oxygen defects were found to cause less structural distortion in SnO than the Sn defects. For the oxygen vacancy, Fig. 6(b), in fact there is no significant structural distortion in the cell. For the oxygen interstitial defect, Fig. 6(d), the only significant distortion is seen for the Sn atom it bonds to, displacing it into the layer by 0.322 Å. This displacement causes a subsequent reduction in the surrounding Sn–O bond lengths by 0.156 Å. The resulting bond length between the Sn and the O interstitial atom is 1.910 Å, which is shorter than the normal Sn–O bond length found away from the defect site. When a Sn atom is removed from the cell, Fig. 6(c), the surrounding four O atoms in the same layer relax away from the vacancy site by 0.243 Å. This relaxation gives rise to a reduction of the Sn–O bonds for these O atoms by 0.101 Å. The final defect, the Sn interstitial, causes a more significant distortion to the layers, Fig. 6(e). The interstitial has five Sn atoms nearest-neighbour to it, forming a square-based pyramid. The layer containing the vertex of this pyramid, layer 1, shows a displacement of the Sn and O atoms away from the Sn interstitial by 0.919 and 0.459 Å, respectively. In the layer containing the base of the pyramid, layer 2, the Sn and O atoms move away from the interstitial by slightly less, 0.251 and 0.291 Å, respectively. The distances between the Sn interstitial and the neighbouring Sn atoms, 2.641 and 2.943 Å for layers 1 and 2 respectively, are significantly shorter than that observed within the rest of the lattice, 3.538 and 3.701 Å for the in-layer and across-layer distances. Comparison with the structural data computed with PBE-vdW[76] shows very close agreement, suggesting that the PBE0-vdW approach has little effect on structural prediction of defective cells relative to PBE-vdW.

To determine the defect formation energies, *via* eqn (5), the range of Sn and O chemical potentials that SnO is stable over needs to be computed. These chemical potentials represent the

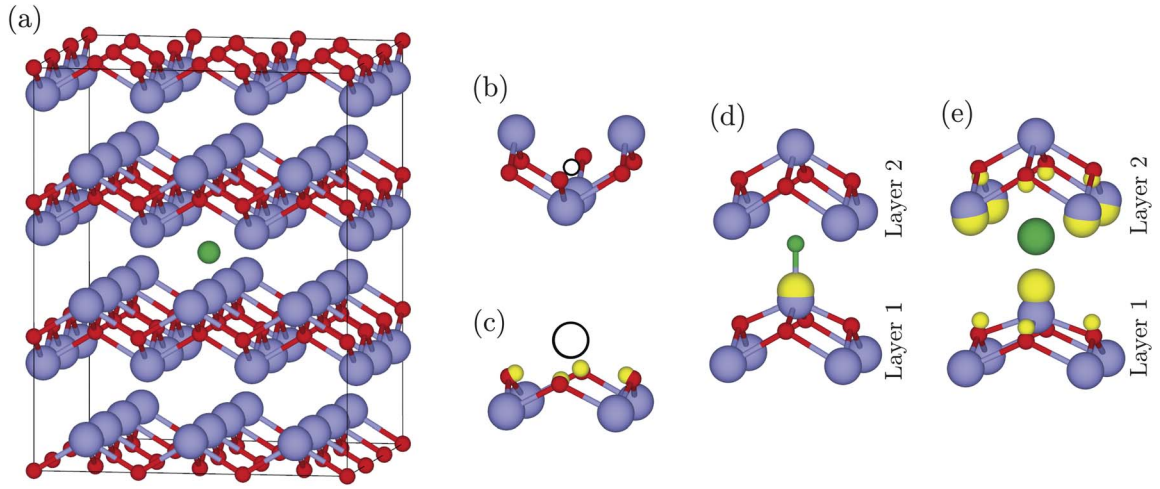


**Fig. 6** Relaxed local atomic structure of the intrinsic defects in SnO using PBE0-vdW. The full 3 × 3 × 3 supercell is shown in (a), with the interstitial site indicated by the green sphere. The modelled defects are (b) oxygen vacancy, (c) tin vacancy, (d) oxygen interstitial and (e) tin interstitial. Tin and oxygen atoms are represented by the large blue and small red spheres, respectively, while the green spheres and black circles indicate interstitials atoms and vacant sites, respectively. Yellow spheres indicate the original supercell positions of any displaced atoms.

**Table 3** PBEo-vdW-calculated bond distances and atomic displacements following intrinsic defect formation in SnO, as well as comparative PBE-vdW-calculated[76] values for the Sn vacancy and O interstitial. All values are given in Å. No values are given for an O vacancy as the defect did not result in any significant structural changes. Layers 1 and 2 refer to those indicated in Fig. 6.† Indicates that the value quoted is the mean over all related distances

| Defect type | Distance | PBE0-vdW | PBE-vdW[76] |
|---|---|---|---|
| O interstitial | Sn displacement | 0.322 | 0.318 |
| | $O_i$–$Sn_{layar\ 1}$ | 1.910 | 1.920 |
| | $O_i \cdots Sn_{layar\ 2}$† | 2.767 | 2.760 |
| | Sn–O (layer 1)† | 2.066 | 2.071 |
| Sn vacancy | O displacements† | 0.243 | 0.232 |
| | Sn–O | 2.121 | 2.122 |
| Sn interstitial | $Sn_{layar\ 1}$ displacement | 0.919 | — |
| | $Sn_{layar\ 2}$ displacements† | 0.251 | — |
| | $O_{layar\ 1}$ displacements† | 0.459 | — |
| | $O_{layar\ 2}$ displacements† | 0.291 | — |
| | $Sn_i \cdots Sn_{layar\ 1}$ | 2.641 | — |
| | $Sn_i \cdots Sn_{layar\ 2}$† | 2.943 | — |
| | $Sn_i \cdots O_{layar\ 1}$† | 3.860 | — |
| | $Sn_i \cdots O_{layar\ 2}$† | 2.985 | — |
| | Sn–O (layer 1)† | 2.077 | — |
| | Sn–O (layer 2)† | 2.275 | — |

growth conditions within the global constraint of the enthalpy of formation of SnO, $\Delta H_f^{SnO}$:

$$\mu_{Sn} + \mu_O = \Delta H_f^{SnO} \quad (9)$$

At the boundary with the metal, typically referred to as Sn-rich/O-poor, the limit is defined by:

$$\mu_{Sn} = 0.00\ \text{eV} \quad (10)$$

$$\mu_O = \Delta H_f^{SnO} \quad (11)$$

The O-rich limit is defined by the formation of $SnO_2$ and therefore has the constraint:

$$\mu_{Sn} + 2\mu_O \leq \Delta H_f^{SnO_2} \quad (12)$$

By using eqn (9) and (12), the chemical potentials at the Sn-poor/O-rich limit can be obtained by:

$$\mu_{Sn} + 2\Delta H_f^{SnO} - \Delta H_f^{SnO_2} \quad (13)$$

$$\mu_O = \Delta H_f^{SnO_2} - \Delta H_f^{SnO} \quad (14)$$

Experimental studies give the formation energies of SnO and $SnO_2$ as −2.96 and −6.02 eV, respectively.[157] Substitution of these values into eqn (13) and (14) gives values for $\mu_{Sn}$ and $\mu_O$ of 0.09 and −3.06 eV. The positive $\mu_O$ value implies that SnO has no thermodynamic stability field, which is consistent with its metastability.[86,87] Consequently, this means that it is not possible to define rich and poor limits for Sn and O. In contrast to the experimental results, a standard PBE methodology does allow a narrow stability field to be defined. For example, Togo *et al.*[60] and Oba *et al.*[92] defined Sn-rich/O-poor and Sn-poor/O-rich chemical limits in their study using the same approach as described by eqn (9)–(14). At the Sn-poor/O-rich limit, they calculated $\mu_{Sn}$ and $\mu_O$ values of −0.23 and −2.49 eV, respectively. Similar results are obtained from our previously calculated PBE formation energies.[76] PBE0 was also found to give an extremely narrow stability field for SnO, with $\mu_{Sn}$ and $\mu_O$ values of −0.04 and −2.59 eV, respectively, at the Sn-poor/O-rich limit. However, previous studies[158–160] have suggested that it is not appropriate to use an erroneous stability field when it is in disagreement with the experimental results, and, regardless, the predicted stability field is so small that it would have little effect on any results. Both the PBE-vdW and PBE0-vdW methodologies, however, agree with experiment by giving positive values of $\mu_{Sn}$ at the Sn-poor/O-rich limit. The lack of a stability field, in-line with experiment, makes it difficult to calculate

 

defect formation energies, as the chemical potentials are required in eqn (5). In our previous PBE-vdW study,[76] we elected to calculate these at the boundary between α-Sn metal and $SnO_2$. *i.e.* when $\mu_{Sn}$ is equal to 0.00 eV. This is therefore used initially, with the corresponding value of $\mu_O$ being −2.65 eV, as this is the PBE0-vdW-calculated $\Delta H_f^{SnO}$.

The defect formation energies for the neutral and charged defects, along with the thermodynamic transition levels between different charge states, are shown for the α-Sn/$SnO_2$ limit in Fig. 7(a). For the p-type defects, the formation energies for a neutral Sn vacancy ($V_{Sn}$) and an oxygen interstitial ($O_i$) are 1.56 and 1.19 eV, respectively. As the energy difference between these two defects is small, both defects would likely be present in experimental samples. However, while the $O_i$ remains in its neutral state within the band gap range, the $V_{Sn}$ does not. The $\varepsilon_D(0/-1)$ transition level is observed 0.39 eV above the VBM. This implies, in agreement with the conclusions of Togo *et al.*[60] and Oba *et al.*,[92] that the observed p-type conductivity is a result of Sn vacancies, not the oxygen interstitials. For a defect to act as a source of conductivity, it must have the transition between charge states close to the VB (p-type) or the CB (n-type). The position of the acceptor states in the band gap (0.39 eV) is in reasonable agreement with photoelectron spectroscopy results which place the Fermi level 0.1–0.2 eV above the VBM.[54] With regards to the n-type defects at this chemical potential limit, the Sn interstitial ($Sn_i$) is seen to have transition levels within the band gap, 0.24 and 0.49 eV below the CBM for the 0/+1 and +1/+2 transitions, respectively; however its high defect formation energy of 4.25 eV means that its concentration will be low and unlikely to play any significant effect. The formation energy of the O vacancy ($V_O$), however, is seen to be considerably lower, at 1.37 eV. The transition levels for $V_O$ donor-states are below the VBM though, meaning that it would not result in n-type conductivity, similar to that seen in $Cu_2O$.[121,127,161] Despite not having any transition levels within the band gap, the similar formation energy as the p-type defects means that it could limit $E_{Fermi}$ from reducing below the top of the VB, limiting hole concentration and conductivity.

The defect character described at the α-Sn/$SnO_2$ limit is in contrast with the experimental observation of good p-type conductivity. In addition, the chemical potentials given at the α-Sn/$SnO_2$ limit are not consistent with the observed Sn-deficiency/O-excess observed in experimental thin films. Therefore, to further understand the effect of the chemical potential on the defect properties of SnO, they were adjusted so that $\mu_{Sn} = \mu_O$. The resultant transition level diagram for this is given in Fig. 7(b). Although the position of the transition levels is not dependent on the chemical potential, the formation energies are. From the α-Sn/$SnO_2$ limit, the decrease in $\mu_{Sn}$ and the increase in $\mu_O$ causes a stabilization of p-type defects and a corresponding destabilization of the n-type defects. Thus the formation energies for $V_O$ and $Sn_i$ become 2.70 and 5.58 eV, respectively; while those for $V_{Sn}$ and $O_i$ reduce to 0.24 and −0.14 eV. This chemical potential range therefore means that the $V_O$ would no longer be likely to pin $E_{Fermi}$ as its concentration would be too low to be significant. However, the formation energy of the $O_i$ becomes negative, indicating spontaneous formation, which is undesirable as it would ultimately move away from the metastability of SnO and lead to the formation of $SnO_2$.

A third set of chemical potentials were therefore trialled, the transition level diagram for which is detailed in Fig. 7(c). These chemical potentials, where $\mu_{Sn}$ and $\mu_O$ were set to −1.00 and −1.65 eV, respectively, were adjusted to give conditions which favour small, positive defect formation energies for the p-type

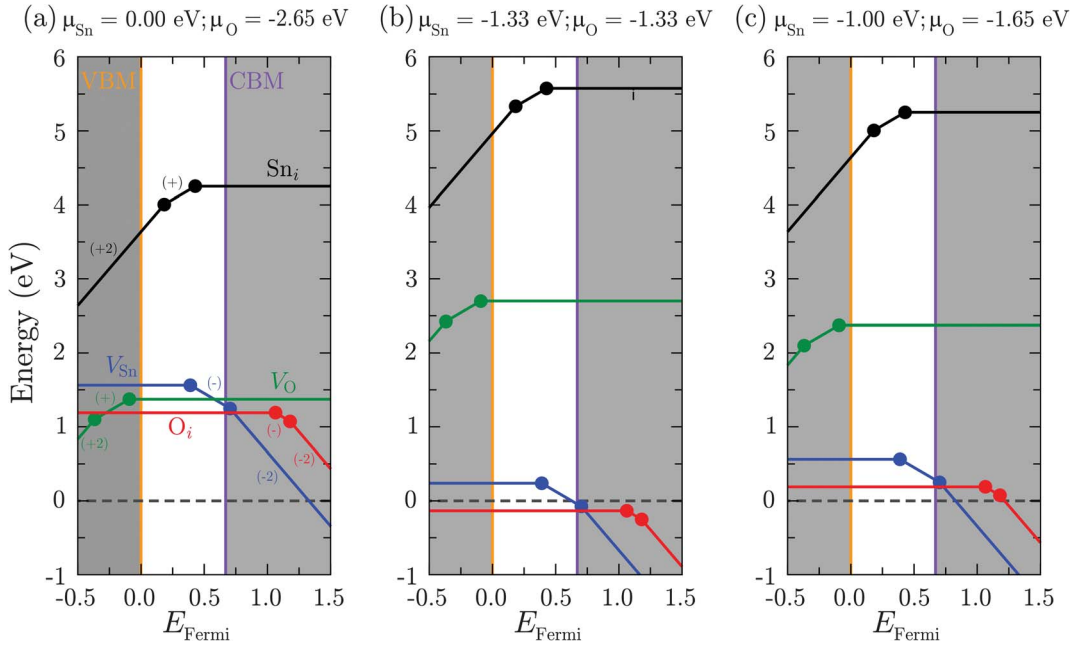


**Fig. 7** Transition level diagrams for the intrinsic defects of SnO under differing conditions, where the Sn chemical potential is set to (a) 0.00 eV (*i.e.* the boundary between α-Sn metal and $SnO_2$), (b) −1.33 and (c) −1.00 eV.

defects (desirable for a good p-type conductor). The defect formation energies for the corresponding $V_{Sn}$ and $O_i$ are 0.56 and 0.19 eV, respectively, while those for the $V_O$ and $Sn_i$ are 2.37 and 5.25 eV, respectively. These chemical potentials therefore describe a system which would show good p-type conduction properties *via* the formation of charged Sn vacancies, without the holes being compensated by the n-type defects. Experimental conditions which mimic these chemical potentials should thus lead to a thin film with reasonable p-type character.

The metastability of SnO makes the definition of chemical potentials, and hence the resultant thermodynamic defect chemistry, difficult. However, the results above indicate that the control of the growth conditions can be hugely important for the resultant conduction properties of the thin films. Epitaxial SnO films formed using PLD are typically grown at reduced partial pressures of $O_2$ ($4 \times 10^{-2}$ Pa) and slightly elevated temperatures (575 °C),[5,54] which would act to reduce $\mu_O$ relative to $\mu_{Sn}$. The low partial pressure of $O_2$ is required for SnO growth as high partial pressures lead to the formation of $SnO_2$. Once SnO is generated, it may be possible to increase the partial pressure to enhance the formation of p-type defects. Although the direct computation of a partial pressure from chemical potentials is not possible without the assumption of a fixed Sn chemical potential,[162] contradicting eqn (9), the results of this study are consistent with experiment.

## 4 Discussion

The central aim of this study was twofold: (i) to demonstrate the use of a hybrid-DFT methodology with dispersion corrections for the accurate modelling of SnO, and (ii) to provide an accurate description of the native intrinsic defects of SnO. For the first objective, the PBE0-vdW was found to give an excellent reproduction of the atomic structure of SnO, with similar differences to experiment as had been observed previously with a PBE-vdW method.[76] Of importance are the *c*/*a* ratio and the fractional coordinate of the Sn atom, both of which were very close to experiment. Comparison of the PBE0-predicted cell further demonstrated the need for the dispersion corrections, as while it gave improvements over the standard-PBE approach, it still gave a distorted cell. The area that the PBE0-vdW method provided significant improvement over PBE-vdW was in the electronic structure. While PBE-vdW underestimated both the indirect and direct fundamental band gaps in SnO, PBE0-vdW reproduced the experimental values with little error. This demonstrates that not only are dispersion corrections essential for modelling a material such as SnO, but also an approach that ensures the correct electronic structure is needed, such as hybrid-DFT.

The defect chemistry of SnO was previously considered by Togo *et al.*[60] and Oba *et al.*[92] using a PBE methodology. The defect formation energies that they determined at the Sn-rich/O-poor limit, based on an erroneous stability field, can therefore be compared to those determined in this study at the Sn metal/$SnO_2$ boundary (where $\mu_{Sn} = 0$ eV). For the p-type defects, the PBE0-vdW formation energies for the $V_{Sn}$ and $O_i$ were 1.42 and 1.20 eV, respectively. Very close agreement is observed with those reported by Togo *et al.*, their respective energies being ~1.5 and ~1.2 eV. While they also predicted the $O_i$ to remain unionised, a more significant discrepancy is observed when contrasting the transition levels they predict for the $V_{Sn}$. Due to their severely underestimated band gap (0.29 eV) and GGA methodology, they predict the $\varepsilon_D(0/-1)$ and $\varepsilon_D(-1/-2)$ positions to be approximately 0.03 and 0.08 eV, respectively, above the VBM. This is considerably shallower than PBE0-vdW predicts, which places the $\varepsilon_D(0/-1)$ level 0.39 eV above the VBM.

For the n-type defects, even more discrepancy is observed. Firstly, the defect formation energies of Togo *et al.* are lower, with their results actually predicting $V_O$ to possess the lowest formation energy of all of the intrinsic defects. They also predict the formation of donor states in the band gap, with $\varepsilon_D(+2/+1)$ and $\varepsilon_D(+1/0)$ levels at approximately 0.13 and 0.11 eV below the CBM, respectively, indicating that the n-type defect would dominate. At conditions they term 'O-rich/Sn-poor' ($\mu_{Sn} = -0.23$ eV; $\mu_O = -2.49$ eV), the formation energy for the $V_O$ is still predicted to be comparable to the $V_{Sn}$, meaning that they will likely still compete with the p-type defects. To compensate for the under-predicted band gap, both Togo *et al.* and Oba *et al.* applied a rigid shift to their CBM and $V_O$ transition levels. However, the results still described a system where the acceptor and donor-states would cancel. Oba *et al.* did estimate a higher formation energy for $V_O$, but predicted an $\varepsilon_D(+2/0)$ level ~0.12 eV below the CBM (within a 0.7 eV band gap), with the charged $V_O$ states crossing with the charged $V_{Sn}$ line which would result in a pinning of the Fermi level ~0.1 eV above the VBM. As the change in conditions, and hence chemical potential, affects only the defect formation energy and not the position of transition levels, this means that the material would be insulating under all conditions. This description is clearly in contrast to the experimentally-observed p-type conductivity. The deficiencies in the GGA-predicted transition level diagram are a direct result of the method used, which gives more delocalised electrons, and hence shallow states and lower formation energies. This therefore further illustrates the requirement of a hybrid-DFT approach for accurately modelling the defect properties of SnO, such as the PBE0-vdW methodology presented here.

It is also instructive to compare the calculated transition levels of this study with those predicted for other p-type materials, in an effort to gauge the effectiveness of SnO. $Cu_2O$,[94] $CuAlO_2$ (ref. 28) and $CuCrO_2$ (ref. 23) have all had detailed studies made of their defect chemistry to elucidate their p-type properties. The dominant intrinsic defect in all three materials is the Cu vacancy. In $Cu_2O$, there are two forms of the vacancy with similar formation energies, the simple vacancy and a 'split' vacancy where a copper ion in a nearest-neighbour position moves to be equidistant between its position and the vacancy. These two defects exhibit reasonably deep $\varepsilon_D(0/-1)$ levels 0.22 and 0.47 eV above the VBM. Of the Cu-based delafossites $CuAlO_2$ and $CuCrO_2$, the latter has been shown to possess a higher undoped conductivity, with reported hole mobilities of 11 $cm^2\ V^{-1}\ s^{-1}$ and carrier concentrations of $4.75 \times 10^{17}$ $cm^{-3}$.[163] The $\varepsilon_D(0/-1)$ transitions for the Cu vacancy in $CuCrO_2$ and $CuAlO_2$ are found to be 0.37 and 0.68 eV above the VBM, respectively. The acceptor levels in SnO are predicted to be 0.39 eV above the VBM. This indicates that whilst the transition is not shallow, it is comparable with $CuCrO_2$,

 

which is currently the best p-type transparent conducting oxide and has attracted attention for p-type devices, with doping used to enhance the conductivity and reduce its high inherent resistivity. SnO is thus suggested to be at least comparable to the present generation of materials which are being investigated for use in p-type devices. Although the formation energy for the Sn interstitial defect is predicted to be high, the $\varepsilon_D(+1/0)$ level is observed 0.24 eV below the CBM. In contrast, the dominant intrinsic defects in the n-type semiconductors ZnO and $SnO_2$ are O vacancies, which exhibit deep +2/0 levels 1.23 and ~0.9 eV below their respective CBMs,[12,92] and thus require doping. Similar intrinsic defects are seen in SnO which would indicate that donor doping would be therefore required to make n-type SnO, which is consistent with its low CB edge.[80]

## 5 Conclusions

This study has detailed how the coupling of a hybrid-DFT methodology with empirical dispersion corrections can give rise to the accurate prediction of both the atomic and electronic structure of SnO. Specifically this was achieved with a PBE0-vdW approach, with 15% Fock exchange. Analysis of the electronic structure, in addition to comparison with experimental spectra, shows that the top of the VB is primarily comprised of Sn s and O p states, while the unoccupied Sn p states dominated the bottom of the CB. An indirect fundamental band gap is found of 0.67 eV with a direct fundamental gap of 2.7 eV. The optical band gap is calculated as ~2.9 eV which explains the near-transparency of SnO thin films.

The PBE0-vdW methodology has been utilized to carry out a detailed study of the intrinsic defects of SnO to investigate its p-type and n-type conduction properties. As the definition of appropriate chemical potential limits is made difficult due to the lack of a thermodynamic stability field, the defects have been assessed at three different limits to understand the effect of the growth conditions. Overall, the results indicate that n-type conductivity will not arise from the intrinsic dopants, due to high $Sn_i$ formation energy and the $V_O$ remaining unionised within the band gap. The p-type defects are observed to have similar, low formation energies, however, the $O_i$ is found to be unionised within the band gap and thus not a source of p-type conductivity. The p-type properties instead arise form the $V_{Sn}$, which shows a $0/-1$ transition level 0.39 eV above the VBM. This indicates that whilst the transition level is relatively deep, SnO should, at least, show p-type properties comparable with the best transparent p-type materials, such as $CurO_2$. However, analysis of the effect of chemical potentials on the defect formation energies indicate care must be taken to not stabilize the formation of $V_O$ such that they limit hole formation and hence conductivity.

## Acknowledgements

This work was supported by Science Foundation Ireland through the Principal Investigators program (PI Grant numbers 06/IN.1/I92 and 06/IN.1/I92/EC07). Calculations were performed on the Lonsdale and Kelvin supercomputers as maintained by TCHPC, and the Stoney supercomputer as maintained by ICHEC, and the HECToR supercomputer through membership of the UK's HPC Materials Chemistry Consortium, which is funded by EPSRC grant EP/F067496. D. O. S. is grateful to the Ramsay Memorial Trust and University College London for the provision of a Ramsay Fellowship. L. F. J. P acknowledges support from a Jean-Pierre Mileur Faculty Development Fund Grant.

## References

1 Z. Han, N. Guo, F. Li, W. Zhang, H. Zhao and Y. Qian, *Mater. Lett.*, 2001, **48**, 99–103.
2 A. Odani, A. Nimberger, B. Markovsky, E. Sominski, E. Levi, G. G. Kumar, M. Motiei, A. Gedanken, P. Dan and D. Aurbach, *J. Power Sources*, 2003, **119**, 517–521.
3 J. Calderer, P. Molinàs, J. Suieiras, E. Llobet, X. Vilanova, X. Correig, F. Masana and A. Rodríguez, *Microelectron. Reliab.*, 2000, **40**, 807–810.
4 X. Q. Pan and L. Fu, *J. Electroceram.*, 2001, **7**, 35–46.
5 Y. Ogo, H. Hiramatsu, K. Nomura, H. Yanagi, T. Kamiya, M. Hirano and H. Hosono, *Appl. Phys. Lett.*, 2008, **93**, 032113.
6 K. Nomura, H. Ohta, A. Takagi, T. Kamiya, M. Hirano and H. Hosono, *Nature*, 2004, **432**, 488–492.
7 J. H. Na, M. Kitamura and Y. Arakawa, *Appl. Phys. Lett.*, 2008, **93**, 213505.
8 K. Nomura, T. Aoki, K. Nakamura, T. Kamiya, T. Nakanishi, T. Hasegawa, M. Kimura, T. Kawase, M. Hirano and H. Hosono, *Appl. Phys. Lett.*, 2010, **96**, 263509.
9 H. Yabuta, N. Kaji, R. Hayashi, H. Kumomi, K. Nomura, T. Kamiya, M. Hirano and H. Hosono, *Appl. Phys. Lett.*, 2010, **97**, 072111.
10 A. Walsh, C. R. A. Catlow, M. Miskufova and A. A. Sokol, *J. Phys.: Condens. Matter*, 2011, **23**, 334217.
11 C. R. A. Catlow, A. A. Sokol and A. Walsh, *Chem. Commun.*, 2011, **12**, 3386–3388.
12 D. O. Scanlon and G. W. Watson, *J. Mater. Chem.*, 2012, **22**, 25236–25245.
13 H. Hosono, N. Kikuchi, N. Ueda and H. Kawazoe, *J. Non-Cryst. Solids*, 1996, **198–200**, 165–169.
14 H. Kawazoe, H. Yasakuwa, H. Hyodo, M. Kurita, H. Yanagi and H. Hosono, *Nature*, 1997, **389**, 939–942.
15 H. Kawazoe, H. Yanagi, K. Ueda and H. Hosono, *MRS Bull.*, 2000, **25**, 28–36.
16 H. Hiramatsu, K. Ueda, H. Ohta, M. Orita, M. Hirano and H. Hosono, *Appl. Phys. Lett.*, 2012, **81**, 598–600.
17 H. Hiramatsu, M. Orita, M. Hirano, K. Ueda and H. Hosono, *J. Appl. Phys.*, 2002, **91**, 9177–9181.
18 K. Ueda and H. Hosono, *Thin Solid Films*, 2002, **411**, 115–118.
19 H. Hiramatsu, K. Ueda, H. Ohta, M. Hirano, T. Kamiya and H. Hosono, *Appl. Phys. Lett.*, 2003, **82**, 1048–1050.
20 M. Snure and A. Tiwari, *Appl. Phys. Lett.*, 2007, **91**, 092123.
21 K. G. Godinho, G. W. Watson, A. Walsh, A. J. H. Green, D. J. Payne, J. Harmer and R. G. Egdell, *J. Mater. Chem.*, 2008, **18**, 2798–2806.

22 T. Arnold, D. J. Payne, A. Bourlange, J. P. Hu, R. G. Egdell, L. F. J. Piper, L. Colakerol, A. De Masi, P. A. Glans, T. Learmonth, K. E. Smith, J. Guo, D. O. Scanlon, A. Walsh, B. J. Morgan and G. W. Watson, *Phys. Rev. B: Condens. Matter Mater. Phys.*, 2009, **79**, 075102.
23 D. O. Scanlon, A. Walsh and G. W. Watson, *Chem. Mater.*, 2009, **21**, 4568–4576.
24 D. O. Scanlon, A. Walsh, B. J. Morgan, G. W. Watson, D. J. Payne and R. G. Egdell, *Phys. Rev. B: Condens. Matter Mater. Phys.*, 2009, **79**, 035101.
25 D. Shin, J. S. Foord, D. J. Payne, T. Arnold, D. J. Aston, R. G. Egdell, K. G. Godinho, D. O. Scanlon, B. J. Morgan, G. W. Watson, E. Mudnier, C. Yaicle, A. Pougier, L. Colakerol, P. A. Glasns, L. F. J. Piper and K. E. Smith, *Phys. Rev. B: Condens. Matter Mater. Phys.*, 2009, **80**, 233105.
26 K. G. Godinho, J. J. Carey, B. J. Morgan, D. O. Scanlon and G. W. Watson, *J. Mater. Chem.*, 2010, **20**, 1086–1096.
27 D. O. Scanlon, K. G. Godinho, B. J. Morgan and G. W. Watson, *J. Chem. Phys.*, 2010, **132**, 024707.
28 D. O. Scanlon and G. W. Watson, *J. Phys. Chem. Lett.*, 2010, **1**, 3195–3199.
29 D. O. Scanlon and G. W. Watson, *J. Mater. Chem.*, 2011, **21**, 3655–3663.
30 K. G. Godinho, B. J. Morgan, J. P. Allen, D. O. Scanlon and G. W. Watson, *J. Phys.: Condens. Matter*, 2011, **23**, 334201.
31 H. Yanagi, T. Hase, S. Ibuki, K. Ueda and H. Hosono, *Appl. Phys. Lett.*, 2001, **78**, 1583–1585.
32 D. J. Payne, R. G. Egdell, A. Walsh, G. W. Watson, J. H. Guo, P. A. Glans, T. Learmonth and K. E. Smith, *Phys. Rev. Lett.*, 2006, **96**, 157403.
33 A. Walsh, D. J. Payne, R. G. Egdell and G. W. Watson, *Chem. Soc. Rev.*, 2011, **40**, 4455–4463.
34 N. V. Sidgwick, *The Electronic Theory of Valency*, Clarendon Press, Oxford, UK., 1927.
35 R. J. Gillespie and R. S. Nyholm, *Q. Rev., Chem. Soc.*, 1957, **11**, 339–380.
36 L. E. Orgel, *J. Chem. Soc.*, 1959, 3815–3819.
37 I. Lefebvre, M. Lannoo, G. Allan, A. Ibanez, J. Fourcade, J. C. Jumas and E. Beaurepaire, *Phys. Rev. Lett.*, 1987, **59**, 2471–2474.
38 G. W. Watson and S. C. Parker, *J. Phys. Chem. B*, 1999, **103**, 1258–1262.
39 G. W. Watson, S. C. Parker and G. Kresse, *Phys. Rev. B: Condens. Matter Mater. Phys.*, 1999, **59**, 8481–8486.
40 G. W. Watson, *J. Chem. Phys.*, 2001, **114**, 758–763.
41 A. Walsh and G. W. Watson, *J. Solid State Chem.*, 2005, **178**, 1422–1428.
42 A. Walsh and G. W. Watson, *J. Phys. Chem. B*, 2005, **109**, 18868–18875.
43 R. Seshadri, G. Baldinozzi, C. Felser and W. Tremel, *J. Mater. Chem.*, 1999, **9**, 2463–2466.
44 R. Seshadri, *Proc. - Indian Acad. Sci., Chem. Sci.*, 2001, **113**, 487–496.
45 R. Seshadri and N. A. Hill, *Chem. Mater.*, 2001, **13**, 2892–2899.
46 J.-M. Raulot, G. Baldinozzi, R. Seshadri and P. Cortona, *Solid State Sci.*, 2002, **4**, 467–474.
47 U. V. Waghmare, S. A. Spaldin, H. C. Kandpal and R. Seshadri, *Phys. Rev. B: Condens. Matter Mater. Phys.*, 2003, **67**, 125111.
48 R. Seshadri, *Solid State Sci.*, 2006, **8**, 259–266.
49 J. Yang and M. Dolg, *Phys. Chem. Chem. Phys.*, 2007, **9**, 2094–2102.
50 A. Walsh, G. W. Watson, D. J. Payne, R. G. Edgell, J. Guo, P.-A. Glans, T. Learmonth and K. E. Smith, *Phys. Rev. B: Condens. Matter Mater. Phys.*, 2006, **73**, 235104.
51 D. J. Payne, R. G. Egdell, D. S. L. Law, P. A. Glans, T. Learmonth, K. E. Smith, J. H. Guo, A. Walsh and G. W. Watson, *J. Mater. Chem.*, 2007, **17**, 267–277.
52 M. W. Stoltzfus, P. M. Woodward, R. Seshadri, J.-H. Klepeis and B. Bursten, *Inorg. Chem.*, 2007, **46**, 3839–3850.
53 E. E. Rodriguez, F. Poineau, A. Llobet, K. Czerwinski, R. Seshadri and A. K. Cheetham, *Inorg. Chem.*, 2008, **47**, 6281–6288.
54 Y. Ogo, H. Hiramatsu, K. Nomura, H. Yanagi, T. Kamiya, M. Kimura, M. Hirano and H. Hosono, *Phys. Status Solidi A*, 2009, **206**, 2187–2191.
55 R. C. Keezer, D. L. Bowman and J. H. Becker, *J. Appl. Phys.*, 1968, **39**, 2062–2066.
56 H. Hiramatsu, H. Yanagi, T. Kamiya, K. Ueda, M. Hirano and H. Hosono, *Chem. Mater.*, 2008, **20**, 326–334.
57 D. J. Payne, M. D. M. Robinson, R. G. Egdell, A. Walsh, J. McNulty, K. E. Smith and L. F. J. Piper, *Appl. Phys. Lett.*, 2011, **98**, 212110.
58 S. Sallis, L. F. J. Piper, J. Francis, J. Tate, H. Hiramatsu, T. Kamiya and H. Hosono, *Phys. Rev. B: Condens. Matter Mater. Phys.*, 2012, **85**, 085207.
59 A. Walsh and G. W. Watson, *Phys. Rev. B: Condens. Matter Mater. Phys.*, 2004, **70**, 235114.
60 A. Togo, F. Oba, I. Tanaka and K. Tatsumi, *Phys. Rev. B: Condens. Matter Mater. Phys.*, 2006, **74**, 195128.
61 W. Koch, E. Jan Baerends and M. C. Holthausen, *A Chemist's Guide to Density Functional Theory*, Wiley-VCH Verlag GmbH, Weinheim, Germany, 2001.
62 J. F. Dobson, K. McLennan, A. Rubio, J. Wang, T. Gould, H. M. Le and B. P. Dinte, *Aust. J. Chem.*, 2001, **54**, 513–527.
63 Q. Wu and W. Yang, *J. Chem. Phys.*, 2002, **116**, 515–524.
64 D. O. Scanlon, A. Walsh, B. J. Morgan and G. W. Watson, *J. Phys. Chem. C*, 2008, **112**, 9903–9911.
65 E. Londero and E. Schröder, *Phys. Rev. B: Condens. Matter Mater. Phys.*, 2010, **82**, 054116.
66 F. Corà, A. Patel, N. M. Harrison, C. Roetti and C. R. A. Catlow, *J. Mater. Chem.*, 1997, **7**, 959–967.
67 D. O. Scanlon, G. W. Watson, D. J. Payne, G. R. Atkinson, R. G. Egdell and D. S. L. Law, *J. Phys. Chem. C*, 2010, **114**, 4636–4645.
68 N. E. Christensen, A. Svane and E. L. Peltzer y Blancá, *Phys. Rev. B: Condens. Matter Mater. Phys.*, 2005, **72**, 014109.
69 L. A. Errico, *Physica B*, 2007, **389**, 140–144.
70 M. Dion, H. Ryberg, E. Schröder, D. C. Langreth and B. I. Lundqvist, *Phys. Rev. Lett.*, 2004, **92**, 246401.
71 S. Grimme, *J. Comput. Chem.*, 2004, **25**, 1463–1473.
72 S. Grimme, *J. Comput. Chem.*, 2006, **27**, 1787–1799.

 

73 S. Grimme, J. Antony, S. Ehrlich and H. Krieg, *J. Chem. Phys.*, 2010, **132**, 154104.
74 Y. Duan, *Phys. Rev. B: Condens. Matter Mater. Phys.*, 2008, **77**, 045332.
75 K. Govaerts, R. Saniz, B. Partoens and D. Lamoen, *Phys. Rev. B: Condens. Matter Mater. Phys.*, 2013, **87**, 235210.
76 J. P. Allen, D. O. Scanlon, S. C. Parker and G. W. Watson, *J. Phys. Chem. C*, 2011, **115**, 19916–19924.
77 R. W. Godby, M. Schlüter and L. J. Sham, *Phys. Rev. Lett.*, 1986, **56**, 2415–2418.
78 H. Hosono, Y. Ogo, H. Yanagi and T. Kamiya, *Electrochem. Solid-State Lett.*, 2011, **14**, H13–H16.
79 K. Nomura, T. Kamiya and H. Hosono, *Adv. Mater.*, 2011, **23**, 3431–3434.
80 N. F. Quackenbush, J. P. Allen, D. O. Scanlon, S. Sallis, J. A. Hewlett, A. S. Nandur, B. Chen, K. E. Smith, C. Weiland, D. A. Fischer, J. Woicik, B. E. White, G. W. Watson and L. F. J. Piper, *Chem. Mater.*, 2013, **25**, 3114–3123.
81 Q.-J. Liu, Z.-T. Liu and L.-P. Feng, *Comput. Mater. Sci.*, 2010, **47**, 1016–1022.
82 J. Zhang, Y. Han, C. Liu, W. Ren, Y. Li, Q. Wang, N. Su, Y. Li, B. Ma, Y. Ma and C. Gao, *J. Phys. Chem. C*, 2011, **115**, 20710–20715.
83 W. Guo, L. Fu, Y. Zhang, K. Zhang, L. Y. Liang, Z. M. Liu, H. T. Cao and X. Q. Pan, *Appl. Phys. Lett.*, 2010, **96**, 042113.
84 L. Y. Liang, Z. M. Liu, H. T. Cao, W. Y. Xu, X. L. Sun, H. Luo and K. Cang, *J. Phys. D: Appl. Phys.*, 2012, **45**, 085101.
85 L. Y. Liang, H. T. Cao, X. B. Chen, Z. M. Liu, F. Zhuge, H. Luo, J. Li, Y. C. Lu and W. Lu, *Appl. Phys. Lett.*, 2012, **100**, 263502.
86 A. G. Sabnis, *J. Vac. Sci. Technol.*, 1978, **15**, 1565–1567.
87 M. Batzill and U. Diebold, *Prog. Surf. Sci.*, 2005, **79**, 47–154.
88 L. Y. Liang, Z. M. Liu, H. T. Cao, Z. Yu, Y. Y. Shi, A. H. Chen, H. Z. Zhang, Y. Q. Fang and X. L. Sun, *J. Electrochem. Soc.*, 2010, **157**, H598–H602.
89 L. Y. Liang, Z. M. Liu, H. T. Cao and X. Q. Pan, *ACS Appl. Mater. Interfaces*, 2010, **2**, 1060–1065.
90 K. Okamura, B. Nasr, R. A. Brand and H. Hahn, *J. Mater. Chem.*, 2012, **22**, 4607–4610.
91 M. S. Moreno, R. F. Egerton, J. J. Rehr and P. A. Midgley, *Phys. Rev. B: Condens. Matter Mater. Phys.*, 2005, **71**, 035103.
92 F. Oba, M. Choi, A. Togo, A. Seko and I. Tanaka, *J. Phys.: Condens. Matter*, 2010, **22**, 384211.
93 D. O. Scanlon, A. Walsh, B. J. Morgan, M. Nolan, J. Fearon and G. W. Watson, *J. Phys. Chem. C*, 2007, **111**, 7971–7979.
94 D. O. Scanlon, B. J. Morgan, G. W. Watson and A. Walsh, *Phys. Rev. Lett.*, 2009, **103**, 096405.
95 D. O. Scanlon, B. J. Morgan and G. W. Watson, *J. Chem. Phys.*, 2009, **131**, 124703.
96 B. J. Morgan, D. O. Scanlon and G. W. Watson, *J. Mater. Chem.*, 2009, **19**, 5175–5178.
97 B. Morgan and G. Watson, *Phys. Rev. B: Condens. Matter Mater. Phys.*, 2009, **80**, 233102.
98 D. O. Scanlon, B. J. Morgan and G. W. Watson, *Phys. Chem. Chem. Phys.*, 2011, **13**, 4279–4284.
99 F. Oba, M. Choi, A. Togo and I. Tanaka, *Sci. Technol. Adv. Mater.*, 2011, **12**, 034302.
100 A. B. Kehoe, D. O. Scanlon and G. W. Watson, *Chem. Mater.*, 2011, **23**, 4464–4468.
101 P. R. L. Keating, D. O. Scanlon, B. J. Morgan, N. M. Galea and G. W. Watson, *J. Phys. Chem. C*, 2012, **116**, 2443–2452.
102 G. Kresse and J. Hafner, *Phys. Rev. B: Condens. Matter Mater. Phys.*, 1994, **49**, 14251–14271.
103 G. Kresse and J. Furthmüller, *Phys. Rev. B: Condens. Matter Mater. Phys.*, 1996, **54**, 11169–11186.
104 P. E. Blöchl, *Phys. Rev. B: Condens. Matter Mater. Phys.*, 1994, **50**, 17953–17979.
105 G. Kresse and D. Joubert, *Phys. Rev. B: Condens. Matter Mater. Phys.*, 1999, **59**, 1758–1775.
106 C. Adamo and V. Barone, *J. Chem. Phys.*, 1999, **110**, 6158–6170.
107 M. Ernzerhof and G. E. Scuseria, *J. Chem. Phys.*, 1999, **110**, 5029–5036.
108 S. Heyd, G. E. Scuseria and M. Ernzerhof, *J. Chem. Phys.*, 2003, **118**, 8207–8215.
109 A. V. Krukau, O. A. Vydrov, A. F. Izmaylov and G. E. Scuseria, *J. Chem.Phys.*, 2006, **125**, 224106.
110 J. P. Perdew, K. Burke and M. Ernzerhof, *Phys. Rev. Lett.*, 1996, **77**, 3865–3868.
111 J. Heyd and G. E. Scuseria, *J. Chem. Phys.*, 2004, **121**, 1187–1192.
112 J. Heyd, J. E. Peralta, G. E. Scuseria and R. L. Martin, *J. Chem. Phys.*, 2005, **123**, 174101.
113 M. Marsman, J. Paier, A. Stroppa and G. Kresse, *J. Phys.: Condens. Matter*, 2008, **20**, 064201.
114 S. Chen, Z. G. Gong, A. Walsh and S. H. Wei, *Appl. Phys. Lett.*, 2009, **94**, 041903.
115 J. P. Allen, D. O. Scanlon and G. W. Watson, *Phys. Rev. B: Condens. Matter Mater. Phys.*, 2010, **81**, 161103(R).
116 J. Paier, R. Asahi, A. Nagoya and G. Kresse, *Phys. Rev. B: Condens. Matter Mater. Phys.*, 2009, **79**, 115126.
117 D. O. Scanlon and G. W. Watson, *Chem. Mater.*, 2009, **21**, 5435–5442.
118 D. O. Scanlon and G. W. Watson, *Appl. Phys. Lett.*, 2010, **97**, 131904.
119 D. J. Temple, A. B. Kehoe, J. P. Allen, G. W. Watson and D. O. Scanlon, *J. Phys. Chem. C*, 2012, **116**, 7334–7340.
120 A. Stroppa and G. Kresse, *Phys. Rev. B: Condens. Matter Mater. Phys.*, 2009, **79**, 201201(R).
121 D. O. Scanlon and G. W. Watson, *J. Phys. Chem. Lett.*, 2010, **1**, 2582–2585.
122 I. D. Prodan, G. E. Scuseria and R. L. Martin, *Phys. Rev. B: Condens. Matter Mater. Phys.*, 2006, **73**, 045104.
123 J. L. F. Da Silva, M. V. Ganduglia-Pirovano, J. Sauer, V. Bayer and G. Kresse, *Phys. Rev. B: Condens. Matter Mater. Phys.*, 2007, **75**, 045121.
124 A. Stroppa and S. Picozzi, *Phys. Chem. Chem. Phys.*, 2010, **12**, 5405–5416.
125 A. Janotti and C. G. Van de Walle, *Phys. Status Solidi B*, 2011, **248**, 799–804.
126 J. B. Varley, H. Peelaers, A. Janotti and C. G. Van de Walle, *J. Phys.: Condens. Matter*, 2011, **23**, 334212.

127 D. O. Scanlon and G. W. Watson, *Phys. Rev. Lett.*, 2011, **106**, 186403.
128 J. B. Varley, A. Janotti, C. Franchini and C. G. Van de Walle, *Phys. Rev. B: Condens. Matter Mater. Phys.*, 2012, **85**, 081109(R).
129 M. Wilson, P. Madden, S. A. Peebles and P. W. Fowler, *Mol. Phys.*, 1996, **88**, 1143–1153.
130 L. Bernasconi, M. Wilson and P. A. Madden, *Comput. Mater. Sci.*, 2001, **22**, 94–98.
131 M. S. Moreno and R. C. Mercader, *Phys. Rev. B: Condens. Matter Mater. Phys.*, 1994, **50**, 9875–9881.
132 F. D. Murnaghan, *Proc. Natl. Acad. Sci. U. S. A.*, 1944, **30**, 244–247.
133 H. J. Monkhorst and J. D. Pack, *Phys. Rev. B: Condens. Matter Mater. Phys.*, 1976, **13**, 5188–5192.
134 M. Gajdos, K. Hummer, G. Kresse, J. Furthmüller and F. Bechstedt, *Phys. Rev. B: Condens. Matter Mater. Phys.*, 2006, **73**, 045112.
135 B. Adolph, J. Furthmüller and F. Beckstedt, *Phys. Rev. B: Condens. Matter Mater. Phys.*, 2001, **63**, 125108.
136 L. E. Ramos, J. Paier, G. Kresse and F. Bechstedt, *Phys. Rev. B: Condens. Matter Mater. Phys.*, 2008, **78**, 195423.
137 J. Paier, M. Marsman and G. Kresse, *Phys. Rev. B: Condens. Matter Mater. Phys.*, 2008, **78**, 121201.
138 X. Nie, S. H. Wei and S. B. Zhang, *Phys. Rev. Lett.*, 2002, **88**, 066405.
139 A. Walsh, J. L. F. Da Silva, Y. Yan, M. M. Al-Jassim and S. H. Wei, *Phys. Rev. B: Condens. Matter Mater. Phys.*, 2009, **79**, 073105.
140 A. Walsh, Y. Yan, M. N. Huda, M. M. Al-Jassim and S. H. Wei, *Chem. Mater.*, 2009, **21**, 547–551.
141 J. P. Allen, M. K. Nilsson, D. O. Scanlon and G. W. Watson, *Phys. Rev. B: Condens. Matter Mater. Phys.*, 2011, **83**, 035207.
142 J. P. Allen, D. O. Scanlon and G. W. Watson, *Phys. Rev. B: Condens. Matter Mater. Phys.*, 2011, **84**, 115141.
143 J. P. Allen, J. J. Carey, A. Walsh, D. O. Scanlon and G. W. Watson, *J. Phys. Chem. C*, 2013, **117**, 14759–14769.
144 K. Momma and F. Izumi, *J. Appl. Crystallogr.*, 2011, **44**, 1272–1276.
145 S. B. Zhang and J. E. Northrup, *Phys. Rev. Lett.*, 1991, **67**, 2339–2342.
146 C. G. Van de Walle and J. Neugebauer, *J. Appl. Phys.*, 2004, **95**, 3851–3879.
147 C. Freysoldt, J. Neugebauer and C. G. Van de Walle, *Phys. Rev. Lett.*, 2009, **102**, 016402.
148 M. Burbano, D. O. Scanlon and G. W. Watson, *J. Am. Chem. Soc.*, 2011, **133**, 15065–15072.
149 C. J. Cramer, *Essentials of Computational Chemistry*, John Wiley & Sons, Ltd., Chichester, UK, 2nd edn, 2004.
150 C. J. Bradley and A. P. Cracknell, *Mathematical Theory of Symmetry in Solids*, Oxford University Press, Oxford, UK, 1972.
151 J. Tauc and A. Menth, *J. Non-Cryst. Solids*, 1972, **8–10**, 569–585.
152 M. Beaudoin, M. Meunier and C. J. Arenault, *Phys. Rev. B: Condens. Matter Mater. Phys.*, 1993, **47**, 2197–2202.
153 G. P. Joshi, N. S. Saxena, R. Mangal, A. Mishra and T. P. Sharma, *Bull. Mater. Sci.*, 2003, **26**, 387–389.
154 N. J. Tharayil, R. Raveendran, A. V. Vaidyan and P. G. Chithra, *Indian J. Eng. Mater. Sci.*, 2008, **15**, 489–496.
155 D. Segev and S. H. Wei, *Phys. Rev. B: Condens. Matter Mater. Phys.*, 2005, **71**, 125129.
156 A. Walsh, J. L. F. Da Silva and S. H. Wei, *Phys. Rev. B: Condens. Matter Mater. Phys.*, 2008, **78**, 075211.
157 J. G. Stark and H. G. Wallace, *Chemistry Data Book*, John Murray Ltd., London, UK, 1982.
158 A. K. Singh, A. Janotti, M. Scheffler and C. G. Van de Walle, *Phys. Rev. Lett.*, 2008, **101**, 055502.
159 J. B. Varley, A. Janotti, A. K. Singh and C. G. Van de Walle, *Phys. Rev. B: Condens. Matter Mater. Phys.*, 2009, **79**, 245206.
160 J. B. Varley, A. Janotti and C. G. Van de Walle, *Phys. Rev. B: Condens. Matter Mater. Phys.*, 2010, **81**, 245216.
161 H. Raebiger, S. Lany and A. Zunger, *Phys. Rev. B: Condens. Matter Mater. Phys.*, 2007, **76**, 045209.
162 M. W. Finnis, A. Y. Lozovoi and A. Alavi, *Annu. Rev. Mater. Res.*, 2005, **35**, 167–207.
163 S. Mahapatra and S. A. Shivashankar, *Chem. Vap. Deposition*, 2003, **9**, 238–240.

 